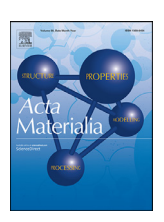
ELSEVIER

Contents lists available at ScienceDirect

Acta Materialia

journal homepage: www.elsevier.com/locate/actamat



Full length article

An experimental and modeling investigation of tensile creep resistance of a stable nanocrystalline alloy



C. Kale^a, S. Srinivasan^a, B.C. Hornbuckle^b, R.K. Koju^c, K. Darling^b, Y. Mishin^{c,*}, K.N. Solanki^{a,*}

- ^a School for Engineering of Matter, Transport, and Energy, Arizona State University, Tempe, AZ 85287, USA
- ^b Army Research Laboratory, Weapons and Materials Research Directorate, Aberdeen Proving Ground, MD 21005, USA
- ^c Department of Physics and Astronomy, George Mason University, MSN 3F3, Fairfax, VA 22030, USA

ARTICLE INFO

Article history:
Received 18 May 2020
Revised 4 August 2020
Accepted 7 August 2020
Available online 18 August 2020

Keywords:
Nanocrystalline
Tensile creep
Transmission electron microscopy
Atomistic simulations

ABSTRACT

Nanocrystalline (NC) materials possess excellent room temperature properties, such as high strength, wear resistance, and toughness as compared to their coarse-grained counterparts. However, due to the excess free energy, NC microstructures are unstable at higher temperatures. Significant grain growth is observed already at moderately low temperatures, limiting the broader applicability of NC materials. Here, we present a design approach that leads to a significant improvement in the high temperature tensile creep resistance (up to 0.64 of the melting temperature) of a NC Cu-Ta alloy. The design approach involves alloying of pure elements to create a distribution of nanometer sized solute clusters within the grains and along the grain boundaries. We demonstrate that the addition of Ta nanoclusters inhibits the migration of grain boundaries at high temperatures and reduces the dislocation motion. This leads to a highly unusual tensile creep behavior, including the absence of any appreciable steady-state creep deformation normally observed in almost all materials. This design strategy can be readily scaled-up for bulk manufacturing of creep-resistant NC parts and transferred to other multicomponent systems such as Ni-based alloys.

© 2020 Acta Materialia Inc. Published by Elsevier Ltd. All rights reserved.

1. Introduction

In coarse-grained (CG) materials, i.e., materials with an average grain size greater than 1000 nm, the creep deformation mechanisms are well known [1] to be dominated by dislocation climb and/or lattice diffusional flow. These mechanisms have been combined in a classical macroscopic treatment, wherein the steady-state creep rate $\dot{\varepsilon}$ under an applied stress σ is given by [1]:

$$\dot{\varepsilon} = AD_0 \exp\left(-\frac{Q}{RT}\right) \left(\frac{Gb}{kT}\right) \left(\frac{b}{d}\right)^p \left(\frac{\sigma}{G}\right)^n,\tag{1}$$

where A is a dimensionless constant, D_0 is the frequency factor, Q is the activation energy of creep, R is the gas constant, T is temperature, G is the at-temperature shear modulus, b is the Burgers vector, k is the Boltzmann constant, d is the average grain size, p is the grain size exponent, and n is the stress exponent. In this classical theory, the value of the stress exponent can be used to distinguish

E-mail addresses: ymishin@gmu.edu (Y. Mishin), kiran.solanki@asu.edu (K.N. Solanki).

between the dominant mechanisms. For instance, the diffusion-based mechanisms of the Nabarro–Herring and Coble creep typically have a smaller stress exponent and stronger grain size dependence as compared to the dislocation-based mechanisms. As such, the Coble creep is observed in materials with finer grain sizes, enabling grain boundary (GB) diffusion at relatively lower temperatures and resulting in higher steady-state creep rates [2]. Accordingly, the steady-state creep rate in many pure nanocrystalline (NC) materials (grain size below 100 nm) was found to be four to five orders of magnitude higher than in CG materials [3–5].

Contrary to the trends mentioned above, it has been recently demonstrated [6] that the compression steady-state creep rate of NC Cu-10at%Ta can be less than 10^{-6} per second — six to eight orders of magnitude lower than that for most NC metals. This drastic retardation of the creep rate was found at temperatures between 0.5 and 0.64 of the melting temperature ($T_{\rm m}$) of the Cu matrix (1,356 K) and under applied stresses ranging from 0.85% to 1.2% of the shear modulus. This unusual combination of properties was made possible via a processing route that created a distribution of nanoclusters of Ta atoms that pinned the GBs within the alloy. The pinning was further shown to improve the thermomechanical stability of the grains by increasing the energy barrier for GB

^{*} Corresponding authors.

sliding and grain rotation and by inhibiting grain coarsening under extremely long-term creep conditions.

However, there is a number of applied and fundamental questions that should be answered for further understanding of the nature of the unusual creep behavior of the Cu-Ta alloys and their potential for applications [7]. The fundamental questions are related to 1) the origin of the large instantaneous strain that exceeds the typically observed strains in other engineering alloys; and 2) the mechanisms responsible for the ability of this material to resist steady-state creep and sustain tertiary creep without fracture under tension loading. The questions related to applications include: 1) The scalability issue, i.e., the ability to control the grain size within a large volume of the material for the production of engineering parts by the appropriate synthesis and consolidation methods; 2) Improvement of the oxidation resistance; and 3) Potential for designing a higher-melting-point analogue of this material for a broader scope of applications, including Ni- or Co-based systems. This paper presents an attempt to address some of these questions.

In this work, a chemically optimized (see Figure S1) NC Cu-3at%Ta alloy (referred to herein as the NC Cu-3Ta alloy) is used as a model material to provide a deeper understanding of the creep response in this highly stabilized system. The optimum Ta solute concentration in the NC Cu-3Ta alloy ensures long-term thermomechanical stability as well as high thermomechanical strength. We apply a combination of experiments and atomistic simulations to study the key mechanisms by which the Ta nanoclusters stabilize the GBs and reduce the tensile creep rates during the primary, secondary, and tertiary stages of the creep process. The understanding gained in this work suggests a clear route to further improvements of the creep resistance of these alloys, as well as the design principles for developing analogous systems for extreme temperature and pressure applications. To demonstrate the transferability of knowledge, we present preliminary work on designing a Ni-based system using a similar approach. Overall, this work demonstrates that properly designed NC materials can be pushed beyond their perceived mechanical and thermal stability limits that were thought to be unbreakable, including the scalability to large mechanical/structural components.

2. Experimental methods and computational details

2.1. Powder processing, machining and test setup

The NC Cu-Ta and Ni-Y alloys were processed using high-energy ball milling followed by equal channel angular extrusion (ECAE). Powders of pure Cu and Ta (-325 mesh and 99.9% purity) were mixed in appropriate amounts and packed in a hardened steel vial under Ar atmosphere. The vial along with the powders was loaded with 440C stainless steel balls with the ball-to-powder ratio of 5:1. The powders were milled at the liquid nitrogen temperature for 4 hours using a SPEXTM milling machine with liquid nitrogen flowing across the vial. Following the milling, the powders were packed in a Ni can under Ar atmosphere (oxygen and $H_2O < 1ppm$) for ECAE processing at 973 K. Further details of the powder processing and ECAE, as well as the impurity characterization can be found in [8]. Similar procedures were followed for the Ni-Y alloy, in which case the ball-to-powder ratio was 10:1 and the cryo-milling time was 8 hours. Before starting the ECAE process, the die assembly used for processing the billets was preheated to 623 K (350°C) to minimize thermal loss during the ECAE processing. The billets, heated and equilibrated to 1373 K (1100°C) for 40 min, were quickly dropped into the ECAE tooling from the furnace and extruded at a rate of 25.5 mm/s.

After the ECAE processing, the Cu-Ta billets were machined on a lathe machine [9] to make cylindrical dogbone samples for performing quasi-static tension and creep experiments (Figure S2).

The samples had threaded grip sections and a gage section with a length of ~ 12 mm and a minimum diameter of ~ 3.3 mm. Tensile creep experiments were performed using an Instron load frame equipped with a 50 kN load cell and an ATSTM clam-shell heating furnace capable of the maximum temperature of 1473 K (1200°C) (Figure S2). The loading rods were machined from MarM 246 (Nibased superalloy) material to avoid any creeping of the setup itself. The creep setup was enclosed by a quartz tube to pass pressurized pure Ar gas (oxygen and H₂O < 1ppm) during the testing (see Figure S2). The quartz tube was sealed at the bottom and the top to avoid any leaks. The system was held at the testing temperature for 30 min before loading to achieve a uniform temperature within the specimen. Creep experiments were carried out at the temperatures of 673 K (0.5 $T_{m})\text{, }873$ K (0.64 $T_{m}\text{), }and 973$ K (0.72 T_m) and various fractions of the at-temperature yield strength (YS). The tests were run for 2 weeks (336 hrs) or until failure. Before performing the tensile creep experiments, quasi-static uniaxial tensile tests were conducted at various temperatures to determine the at-temperature yield strength. The geometry of specimens and the experimental conditions were similar to those for the creep experiments.

2.2. Microstructural characterizations

Transmission Electron Microscopy (TEM) was employed to obtain grain size distributions and microstructural characteristics. TEM characterizations were carried out on as-received and post-deformed samples using an aberration corrected ARM-200F operated at 200 keV. Extensive details on specimen preparation for TEM can be found elsewhere [10–13]. Multiple bright field and dark field images were captured in both the high-resolution TEM and Scanning TEM (STEM) modes to assess the microstructure and quantify statistics such as the grain size distribution. For TEM characterizations of the creep samples, lamellae were prepared in the middle of the gage section (for samples that did not fail) or just below the fracture surfaces (for failed samples).

2.3. Computational details

The atomistic simulations utilized the angular-dependent interatomic potential for the Cu-Ta system [14], which accurately reproduces many properties of this system in agreement with experimental data and first-principles calculations. The molecular dynamics (MD) simulations employed the Large-scale Atomic/Molecular Massively Parallel Simulator (LAMMPS) [15]. The Monte Carlo (MC) simulations were conducted with the parallel MC code ParaGrandMC [16] to generate different compositions of Cu-Ta alloys using the composition–controlled MC algorithm [17]. This algorithm brings the system to thermodynamic equilibrium at a given temperature and the alloy composition under zero–stress conditions.

The Cu nanocrystal was constructed by the Voronoi tessellation method [18] and contained 32 grains with an average grain size of 12.6 nm. The sample contained about 5.4 million atoms and had the approximate dimensions 40 nm x 40 nm x 40 nm with periodic boundary conditions in all directions. Despite the known advantages [18], microstructures created by the Voronoi tessellation method may produce inaccurate time evolution of the grain size distribution. More advanced methods aimed to generate more realistic grain size distributions have been proposed [19–21]. However, in the present work, we only deal with a relatively small number of grains and our goal is not to reproduce their collective time evolution accurately. We are more interested in probing the local creep mechanisms occurring on the scale of a single grain or a small group of grains. The GB structures were optimized by a procedure described in [22]. In the MC simulations, the Ta atoms

Table 1Temperature and stresses (in MPa and fraction of simulated yield stress) implemented in the atomistic simulations.

T (K)	T/ T _m	Simulated Yield stress (MPa)	Applied stress
850	0.64	858	0.35YS (300 MPa)
900	0.68	788	0.38YS (300 MPa)
950	0.72	639	0.47YS (300 MPa)
1000	0.75	554	0.54YS (300 MPa)
1050	0.79	440	0.68YS (300 MPa)
1075	0.81	376	0.80YS (300 MPa)
1100	0.83	338	0.30-0.89YS (100-300 MPa)

were found to precipitate in the form of nano-size clusters located within the grains and at GBs and triple junctions.

To investigate the tensile creep deformation mechanisms, tensile creep simulations were performed by applying a constant stress along one of the Cartesian directions with zero pressure in the lateral directions. The sample was subject to a series of uniaxial stresses ranging from 100 MPa to 300 MPa at temperatures from 850 K to 1100 K. The creep stresses were comparable to those implemented in the experiments. To facilitate comparison with experiments, Table 1 summarizes the simulated creep stresses both in MPa and as a fraction of the at-temperature yield stress. The latter was obtained by separate simulations.

Snapshots of the simulation block were saved at regular intervals of time and were examined using the visualization software OVITO [23]. The atoms in the grains were identified and tracked by utilizing a parallelized C++ computer code written for evaluating the local lattice orientation around each atom [24]. Four different chemical compositions were tested, ranging from pure Cu to Cu-4at% Ta.

3. Results

3.1. Microstructure of the chemically optimized NC material

Initially, the composition of the Cu-Ta alloys was optimized through long-term isothermal annealing experiments and post-annealing hardness measurements on alloys with 1at%, 3at%, 5at%, and 10at% of Ta. The hardness measurements for the four compositions as a function of annealing time at different temperatures have shown that that the NC Cu-3Ta alloy displayed optimum stability at high temperatures for a longer duration (Figure S1). These beneficial properties originate from an optimal interplay among several factors, such as the Ta cluster stability, precipitation hardening effects, and the stability of the average grain size in the matrix [8,25]. This optimized chemical composition was thus chosen for further tensile creep studies.

Fig. 1 shows the as-received microstructure of the NC Cu-3Ta alloy ECAE processed at 973 K. The low magnification bright field (BF) STEM image in Fig. 1A shows the overall microstructure of the alloy. It can be seen that the alloy has Cu grains with an average size of about 100 nm. Ta has a bimodal size distribution: it is present in the form of individual grains with an average diameter of around 50 nm, and as small clusters (<10 nm) with an average diameter of 3 nm. Earlier atom probe studies on Cu1-at%Ta and Cu-10at%Ta showed the Ta cluster densities of about 4.1×10^{23} m^{-3} and 6.5 \times 10²³ m^{-3} , respectively [8]. Higher magnification medium angle annular diffraction (MAADF) STEM images in Cu-3Ta (Fig. 1B) reveal that the Ta nanoclusters are present both inside the Cu grains and along the GBs, and that their number density is on the order of 10^{23} m⁻³. Most of them have a core-shell structure with an oxygen rich core. Note that the powder processing and consolidation are performed in an inert Ar atmosphere with the typical O impurity content less than 1 ppm. Hence, it can be assumed that the majority of oxygen in the clusters comes from the

native oxides in the powders, which are introduced into the lattice during the mechanical alloying. Detailed compositional characterization of Ta nanoclusters can be found in [8]. The Ta clusters are mostly coherent or semi-coherent with the surrounding Cu matrix [26]. The size and inter-particle spacing of the nanoclusters have been shown to remain exceptionally stable under extreme conditions [6,27]. The large Ta particles are very low in density and do not make a significant contribution to the strength of the alloy [28]. Fig. 1C shows the size distribution for the Cu grains having a Gaussian profile with a mean of around 100 nm.

3.2. Mechanical properties and deformed microstructure of the Cu-Ta allov

As discussed in Section 3.1, a series of Cu-Ta alloys with four chemical compositions were prepared and processed at different temperatures for optimization purposes. Fig. 2A shows the true stress - true strain data under uniaxial tensile loading at a strain rate of 0.001 s⁻¹ for different compositions. The solid, dashed and dotted lines correspond to the processing temperatures of 973 K, 1173 K and 1273 K, respectively. For the temperature of 973 K, NC Cu-3Ta (red line) shows significantly improved tensile ductility over other compositions. Based on the improved thermal stability (Figure S1) and tensile ductility, the NC Cu-3Ta alloy was chosen to evaluate high temperature tensile creep behavior. The 0.2% yield strength (YS) of this alloy as a function of temperature, from room temperature (RT, 298 K) up to 973 K, is plotted in Fig. 2B. The alloy exhibits a RT YS of about 955 MPa, which is about twice as high as that of pure NC Cu with similar grain size [29]. Moreover, the YS shows a linear decrease with temperature, as opposed to the sigmoidal dependence seen in CG pure Cu.

Tensile creep experiments were performed under the stress of 0.30 of the yield strength (0.30YS) at 673 K (0.5 T_m), and under 0.30YS and 0.50YS at 873 K (0.64T_m) and 973 K (0.72T_m) using the samples engineered with a backing nut to prevent the slipping of the threads under such extreme conditions (Figure S2). When reporting the test results, the YS is referred to the respective temperature (Fig. 2B). The tensile creep strain as a function of time obtained under the above conditions is plotted in Fig. 3. For comparison, the plot includes the tensile creep data for Ni-based superalloys (mostly single crystals) cited from the literature [30–32]. In the case of NC Cu-3Ta, a prominent primary creep regime can be identified at temperatures up to 873 K $(0.64T_m)$ and for all fractions of the YS. The primary creep is followed by an unusual steady-state creep regime, in which the creep rate becomes nearly zero (the horizontal portion in the curves). The tests were stopped after 2 weeks of testing if no failure occurred. For the test temperature of 973 K (0.72T_m) and all fractions of YS, an extended primary creep regime was observed similar to the one seen at lower temperatures. However, at this temperature the steady-state creep behavior was different, in that it had a non-zero slope and was followed by a short tertiary creep and ultimately failure. The steadystate creep rate at 973 K was on the order of 10^{-8} s⁻¹. In all cases, the time to failure depends on the magnitude of the applied stress. By contrast, Ni-based superalloys show a traditional creep versus time curves where three distinct regimes corresponding to the primary, secondary, and tertiary creep can be identified under all test conditions. The tensile creep behavior exhibited by the NC Cu-3Ta alloy at temperatures up to 0.64T_m is highly unusual for a NC material, especially one that was processed through powder metal-

To further analyze the creep responses, specifically the issue of the large initial strain as discussed in the Introduction, the primary creep strains for all testing conditions were fitted with a power law as presented in Fig. 3B. The strain was found to follow a cubic-root dependence with respect to time $(t^{1/3})$. This behavior is consistent

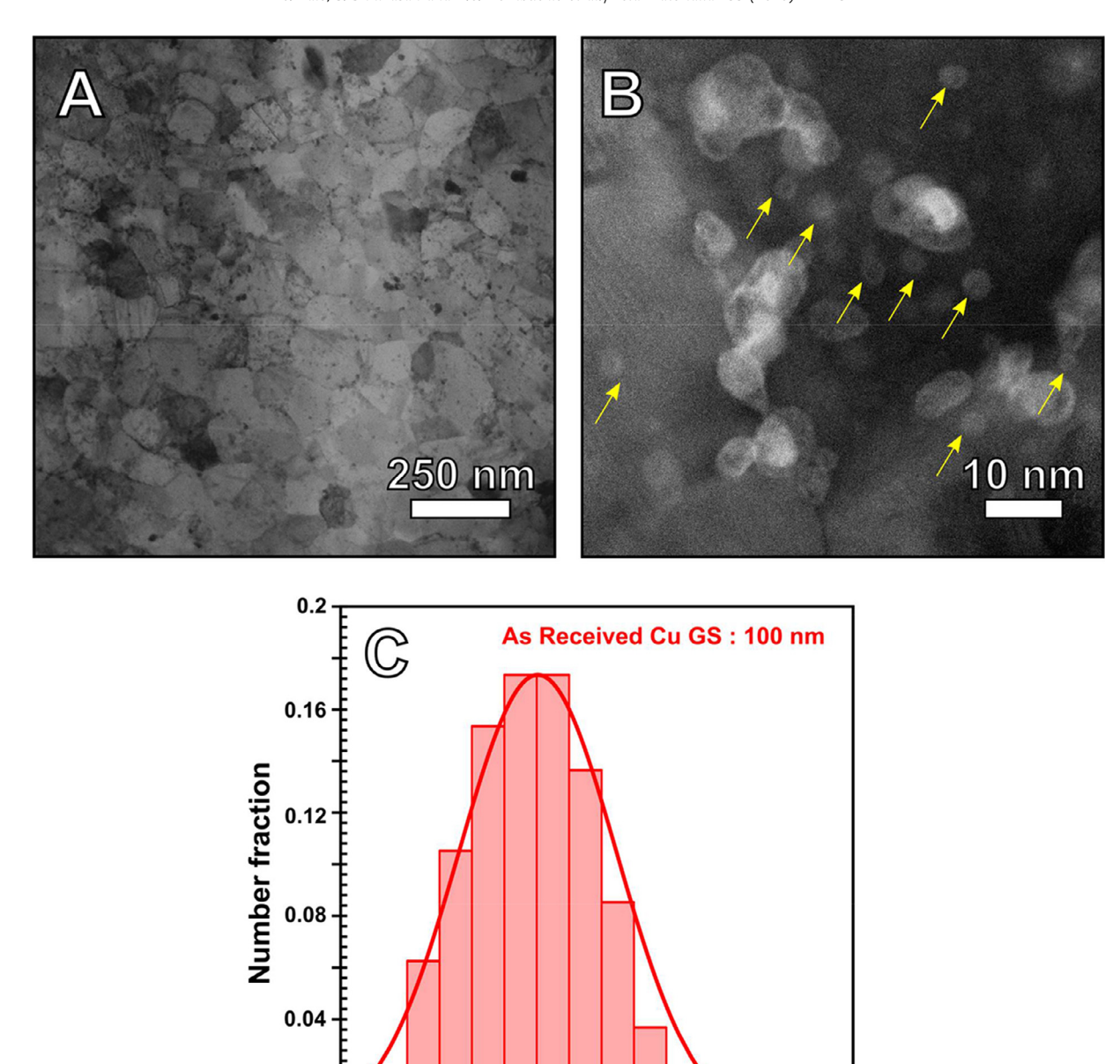


Fig. 1. (A) Bright field (BF) STEM micrograph of as-received NC Cu-3at%Ta showing a low magnification view of the overall microstructure. (B) Medium angle annular dark field (MAADF) STEM micrograph showing a high magnification view of the Ta nanoclusters (marked by yellow arrows). (C) The size distribution of Cu grains in the as-received material.

125

Diameter (nm)

145

165

185

205

105

65

85

with the Andrade β -flow theory [33]. The primary creep is transient in nature and eventually culminates into a steady-state creep behavior. Upon the application of stress, certain regions within the microstructure, for example the GBs and triple junctions, experience stress concentrations. The local stresses in those regions are higher than the applied global stress but lower than the stress required to cause local yielding [34]. As such, the microstructure undergoes relaxation to overcome the local stress buildup, which slows down with time. This relaxation can explain the primary creep deformation observed in NC Cu-3Ta. This explanation is confirmed by the loading and re-loading experiment shown in Fig. 3C. Upon re-loading, the sample crept at 873 K (0.64T_m) for 1.5 weeks displays a lower primary creep strain since the microstructure has already been relaxed during the initial creep testing. This observa-

tion is consistent with the atomistic simulations discussed below. It points to a possible route to reduced initial large instantaneous strain, i.e., annealing under stress to reduce or eliminate the large instantaneous strain. In regard to the limited tertiary creep behavior, this work demonstrates the ability of the microstructure produced by the powder process to withstand damage accumulation and prolong the secondary creep behavior.

Fig. 4 shows low and high magnification BF STEM micrographs of samples creep tested at 873 K ($0.64T_{\rm m}$) and 973 K ($0.72T_{\rm m}$) under a 0.50YS stress. The former specimen lasted for two weeks of testing without failure, whereas the latter one failed after a day of creep testing. Scanning electron microscopy images confirm that a negligible oxide film ($<10\,\mu{\rm m}$ in thickness) was formed on the surface at elevated temperatures, as measured post testing (Figure

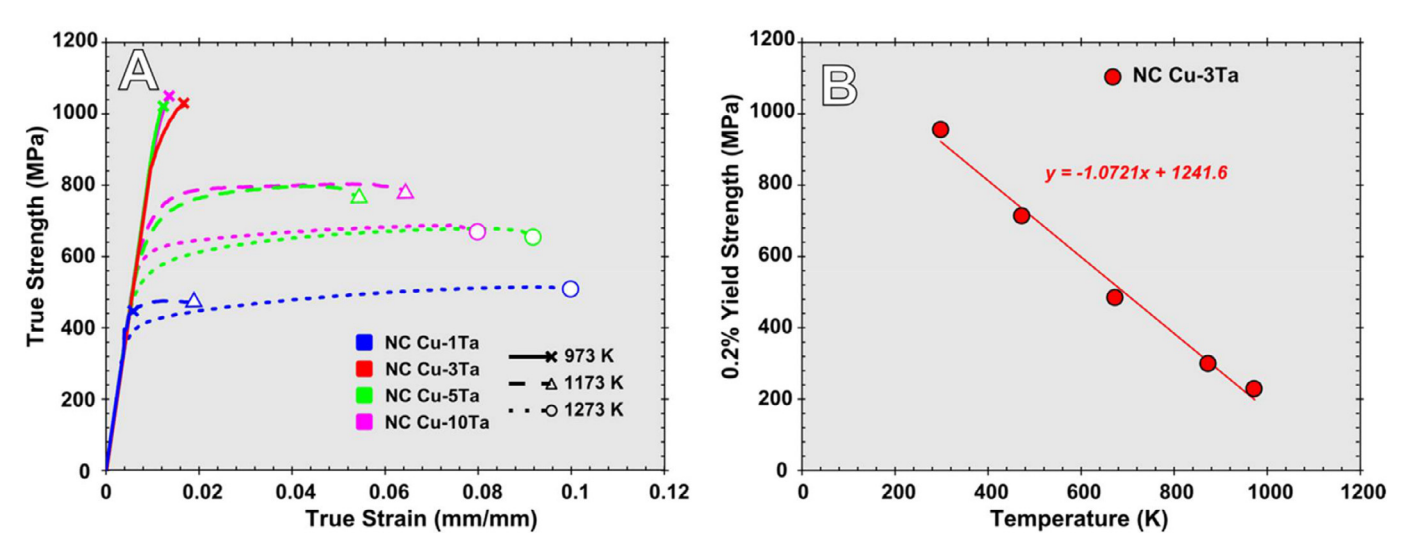


Fig. 2. (A) True stress – true strain data under uniaxial tensile loading at a strain rate of 0.001 s^{-1} for various compositions of the Cu-Ta family (1at%, 3at%, 5at% and 10at% Ta) and processing temperatures (973 K, 1173 K and 1273 K). Strain to failure in each case is indicated by the respective markers. (B) 0.2% Yield strength (YS) obtained by uniaxial tensile tests for the NC Cu-3Ta alloy at a strain-rate of 0.001 s^{-1} as a function of temperature.

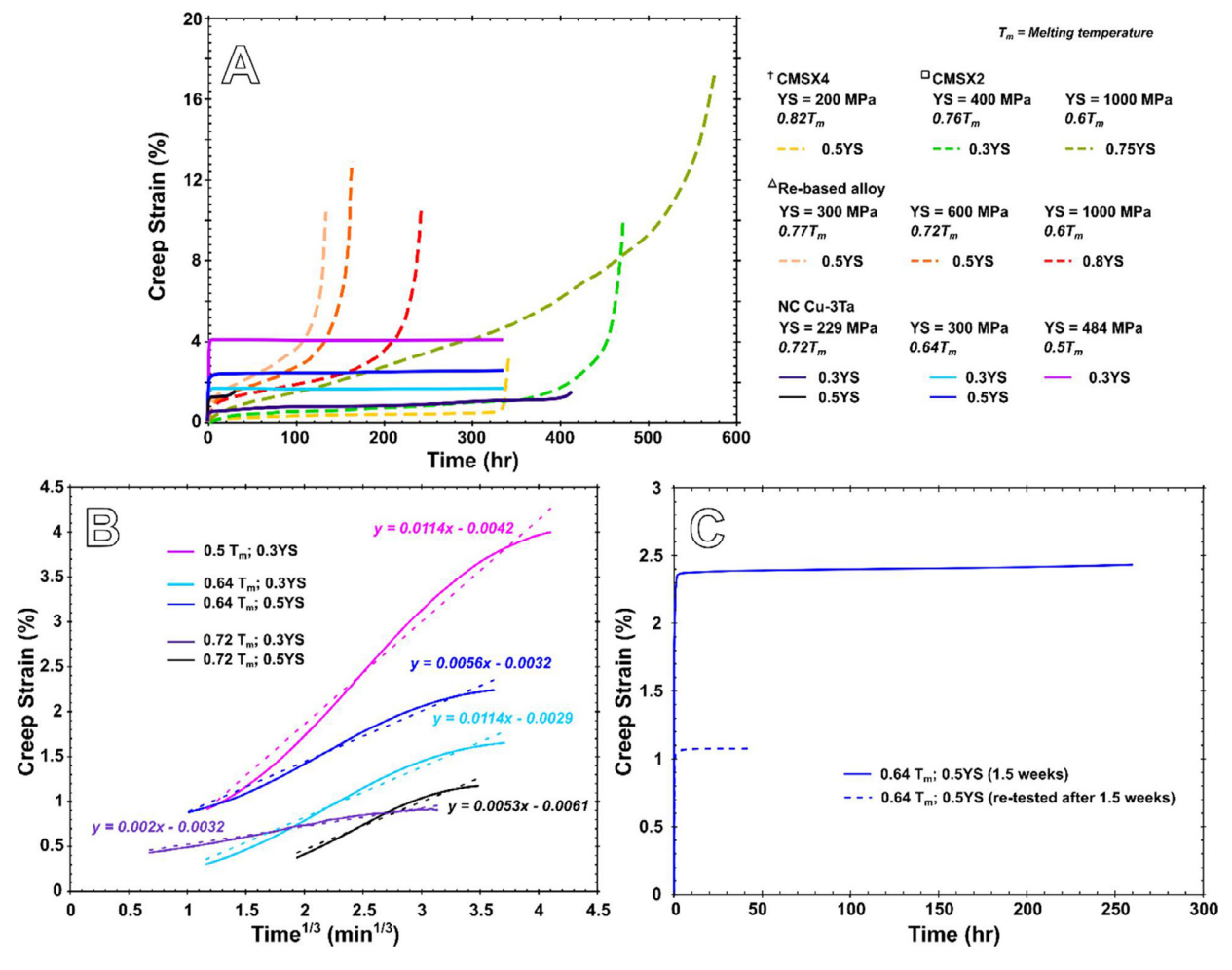


Fig. 3. (A) Tensile creep strain versus time for NC Cu-3at%Ta at different fractions of the melting temperature (T_m) plotted along with data for Ni-based superalloys from the literature [30–32]. (B) Primary creep strain under various testing conditions is plotted as a function of time^{1/3}. (C) Tensile creep curve at 873 K (0.64T_m) and 0.50YS stress for a testing period of 1.5 weeks (solid blue line) followed be re-loading under the same conditions (dotted blue line). Note the reduced primary creep as a result of re-loading.

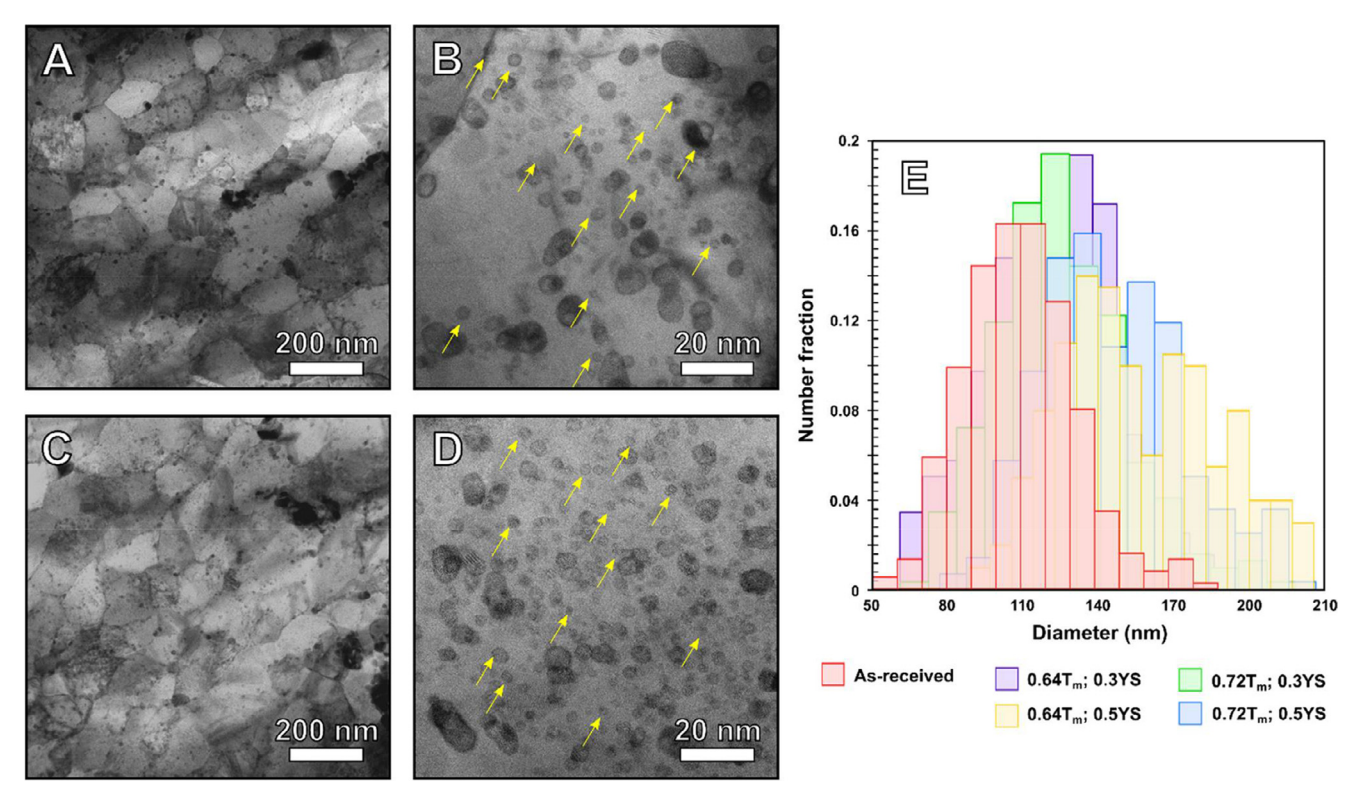


Fig. 4. Bright field (BF) STEM images in (A) and (C) represents the low magnification microstructure for samples creep tested under a 0.5YS stress at 873 K (0.64 T_m) and 973 K (0.72 T_m), respectively. The respective high magnification images are shown in (C) and (D). (E) Size distribution for Cu grains in the as received and creep tested samples at 873 K (0.64 T_m) and 973 K (0.72 T_m) and under various fractions of the YS.

S4). The oxide film formation is likely caused by the increased Ta content in the alloys, creating a native passivation surface layer. This observation suggests a possible pathway for developing oxidation resistant coatings taking advantage of the large density of the interfaces in the material providing fast diffusion paths.

The post-deformed images in Fig. 4 demonstrate that the alloy maintains its NC microstructure even after being subjected to the extreme tensile creep conditions. The size distributions of Cu grains (obtained from multiple micrographs similar to Fig. 4A and C) plotted in Fig. 4E confirm a negligible increase in the grain size as compared to the as-received material. For instance, at 973 K $(0.72T_{\rm m})$ the average Cu grain size is 125 nm, which is only a factor of ~ 1.25 increase relative to the as-received grain size of 100 nm. Under all other testing conditions, the average Cu grain size does not increase beyond 130 nm. The Ta nanoclusters (indicated by yellow arrows in the high magnification images), which are critical in imparting the thermomechanical stability, also show a small change in their average diameter. We can conclude that the slight grain coarsening is only due to the microstructure relaxation during the transient primary creep.

3.3. Atomistic modeling of creep deformation mechanisms

The stress exponent n appearing in Eq. (1) is often used as an indicator of the creep deformation mechanism in materials [35]. However, the highly unusual creep behavior of the NC Cu-3Ta alloy limits our ability to infer the creep mechanism from experimentally measured values of n. More direct investigation methods must be used. In this section, we discuss the results of three-dimensional atomistic computer simulations of the tensile creep process in NC Cu-Ta alloys designed to underpin the dominant creep deformation mechanisms.

The simulations were performed using the MD and MC methods for four different chemical compositions: pure Cu, 0.5at%Ta,

2at%Ta and 4at%Ta. As mentioned above, thermodynamic equilibration of the simulation models resulted in the formation of nanosized Ta clusters distributed inside the Cu grains, at GBs, and near triple junctions, similar to their distribution observed by TEM in as-received samples. Fig. 5 illustrates the microstructure evolution under a 300 MPa creep loading at the temperature of 1100 K in pure NC Cu and the NC Cu-4at%Ta alloy. In pure NC Cu, significant grain growth and grain rotation are observed after 14 ns of creep testing, along with twinning and dislocation emission and propagation. Similar microstructure evolution (not shown here for the sake of brevity) was also observed in samples with the 0.5at%Ta and 2at%Ta compositions. The grain growth was significantly slower but visible. By contrast, simulations of NC Cu-4at%Ta revealed excellent microstructural stability as shown in Fig. 5B. In this alloy, GB migration was strongly impeded by the Ta clusters, drastically slowing down the grain growth and preserving the total number of grains. The simulation block was only found to elongate along the tensile direction and compress in lateral directions.

The deformed microstructure showed evidence of GB sliding and short circuit diffusion along the GBs. Fig. 6 displays the evolution of the network of mutually perpendicular marker lines in the Cu-4.0%Ta alloy after 200 ns of the creep test. Comparing the initial and final snapshots of the structure, we find that the marker lines intersecting with the GBs are segmented and shifted relative to each other, which is a signature of GB sliding. Some of the segments are slightly tilted relative to the original orientation, which is an indication of grain rotation. However, the amount of GB sliding and grain rotation is relatively small. The most prominent feature of these images is the extensive spreading of the material that initially belonged to the marker lines along the GBs. This spreading is direct evidence of extensive GB diffusion occurring during the test. There is no spreading of the marker lines inside the grains, indicating the absence of any appreciable lattice diffusion on the time scale of the simulations.

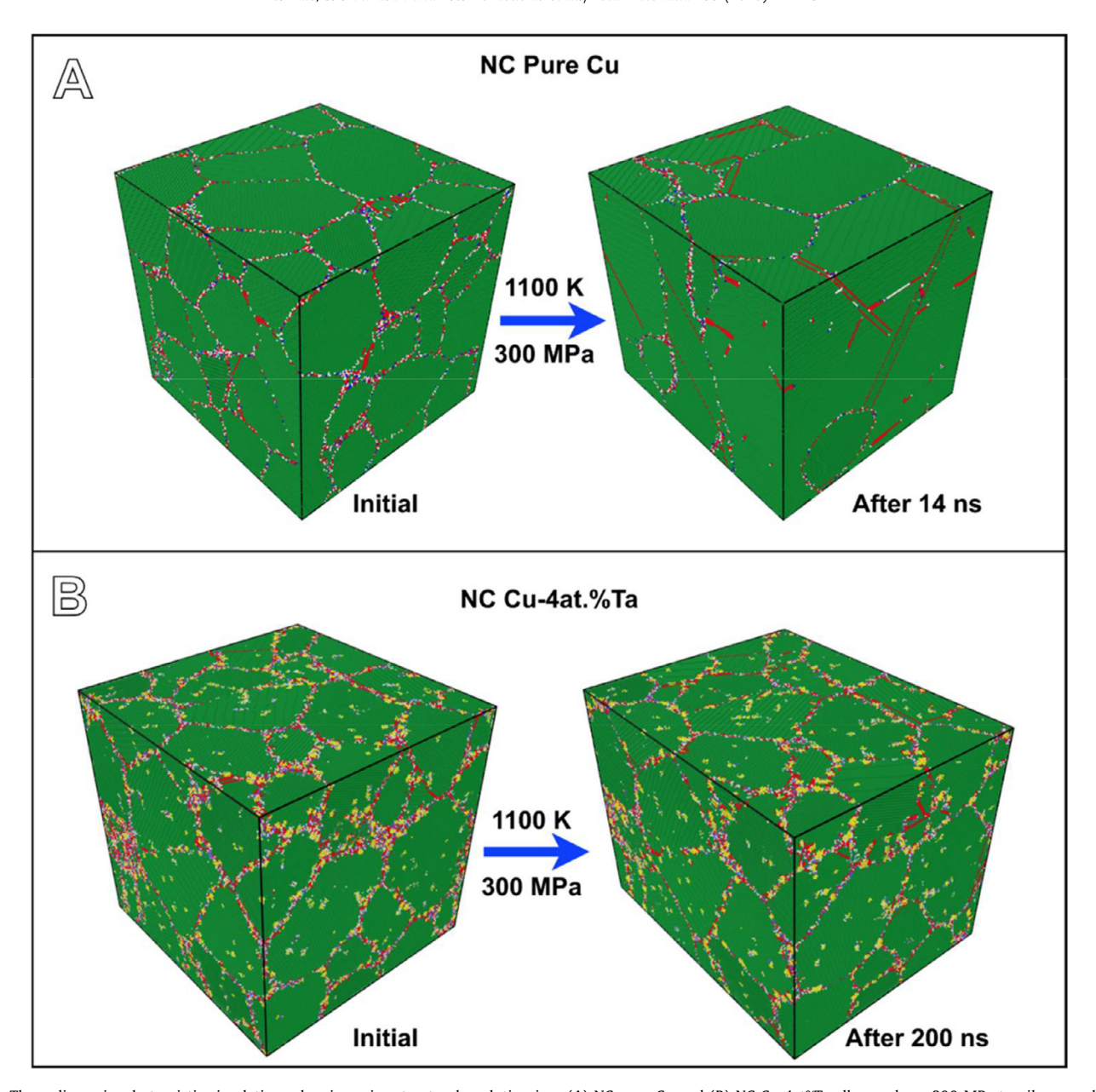


Fig. 5. Three-dimensional atomistic simulations showing microstructural evolution in a (A) NC pure Cu and (B) NC Cu-4at%Ta alloy under a 300 MPa tensile creep loading at 1100 K. The green and yellow colors indicate Cu atoms in perfect FCC environments and Ta atoms, respectively. The remaining colors decorate GBs.

Typical strain-time curves observed in the simulations at different temperatures and stresses are shown in Fig. 7 together with the respective strain-rate plots. The curves display primary and steady-state creep stages with the steady-state creep rate increasing with temperature and stress. From the logarithmic plot of the strain rate versus stress (Fig. 8A), the stress exponent appearing in Eq. (1) was found to be $n=3.8\pm0.4$. The activation energy of creep Q was extracted from the linear fit to the Arrhenius plot shown in Fig. 8B. The activation energy obtained, 1.5 ± 0.2 eV, is smaller than that for lattice diffusion in Cu but higher than typical activation energies of GB diffusion in pure Cu [36,37]. The latter trend points to retardation of GB diffusion due to the presence of Ta clusters, which is one of the important factors in the thermomechanical stability of this alloy.

It should be emphasized the GB diffusion process controlling the diffusional creep requires the motion of both the host (Cu) and solute (Ta) atoms in a concerted manner. The melting temperature of Ta is more than twice as high as that of Cu. Based on the known correlations between GB diffusion and the melting point [37], it is expected that Ta atoms diffuse in GBs much slower than Cu atoms. This must lead to a reduction of the effective GB diffusivity and explains why the creep activation energy in Cu-Ta alloys is higher than that for GB diffusion in pure Cu.

To investigate the creep mechanism in more detail, two-dimensional slices of the three-dimensional simulated structure were examined as shown in Fig. 9. The atoms initially residing in three selected grains are colored in orange for visualization purposes. Fig. 9B reveals that new crystal planes (indicated by cyan arrows) are added on either side of the GBs oriented normal to the tensile direction (arrows in Fig. 9B). At the same time, crystal planes are dissolved near the GBs that are parallel to the tensile direction. Thus, during the creep process, the material is transported from GBs parallel to the tensile direction and accreted to GBs normal to the tensile direction. This mass transport results in elongation of the grains in the tensile direction and thus in tensile creep deformation. Analysis of the atomic movements indicates

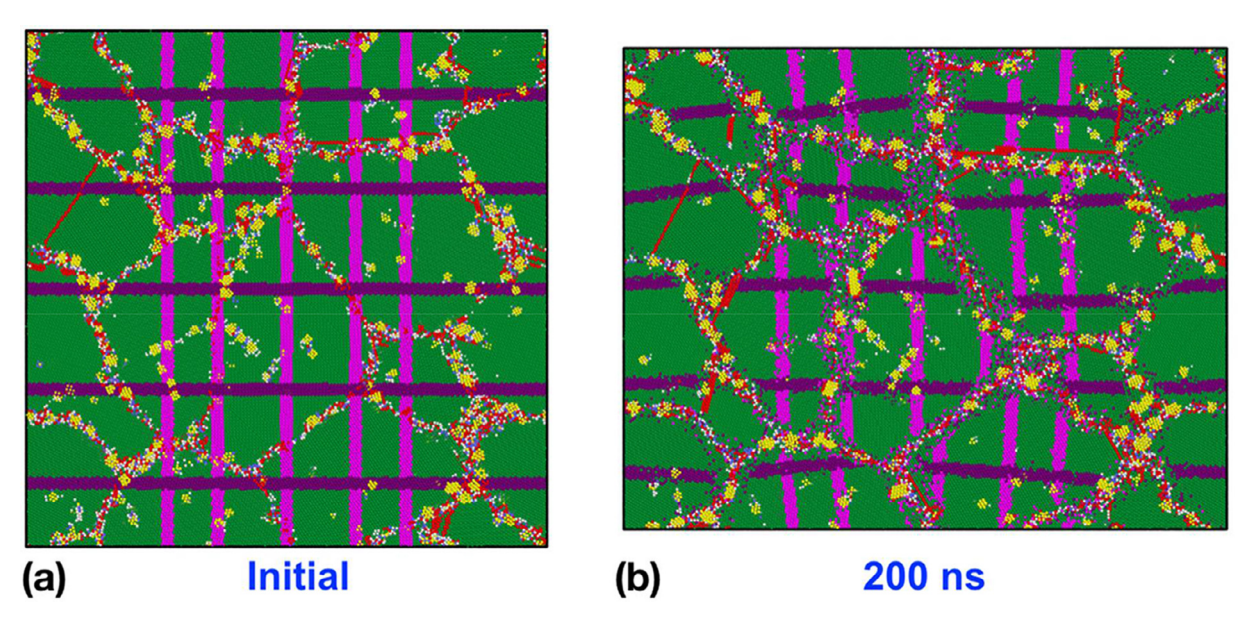


Fig. 6. Cross-sections of the Cu-4at%Ta alloy during simulated tensile creep tests. (a) Initial and (b) final state after tensile creep deformation under a stress of 300 MPa at 1100 K. The tensile creep direction is horizontal. The horizontal (purple) and vertical (pink) stripes are two sets of mutually perpendicular marker lines. FCC, HCP and Ta atoms are colored in green, red, and yellow colors, respectively.

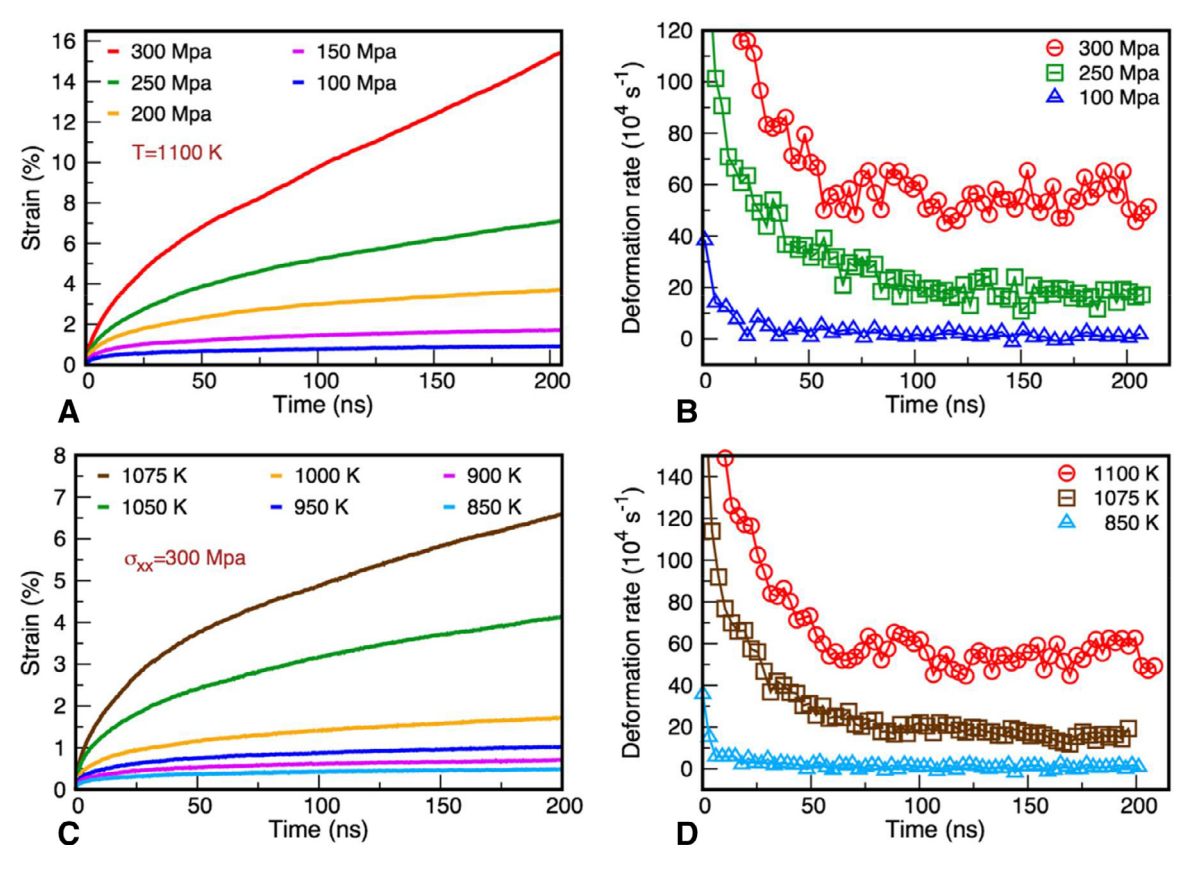


Fig. 7. Strain versus time and strain-rate versus time curves obtained by MD tensile creep simulations at a fixed temperature of 1100 K and different stresses (A,B), and a fixed tensile stress of 300 MPa and different temperatures (C,D).

that mass transport occurs predominantly by diffusion along the GBs. This diffusion process is driven by the difference between the chemical potentials of atoms at differently oriented GBs, which in turn arises from the difference in the normal components of the stress. This deformation mechanism falls under the definition of the Coble creep [2]. Although the simulated grain size is smaller than the experimental, we emphasize that the processes described

have a local character and are expected to occur in larger grains just as well.

To confirm the GB diffusion mechanism of the creep deformation, slip vector analysis was performed on the deformed NC Cu-4at%Ta samples at two temperatures of 900 K and 1100 K, see Fig. 9C-D. It was found that partial dislocations were emitted from the GBs during the deformation process, but were typically ab-

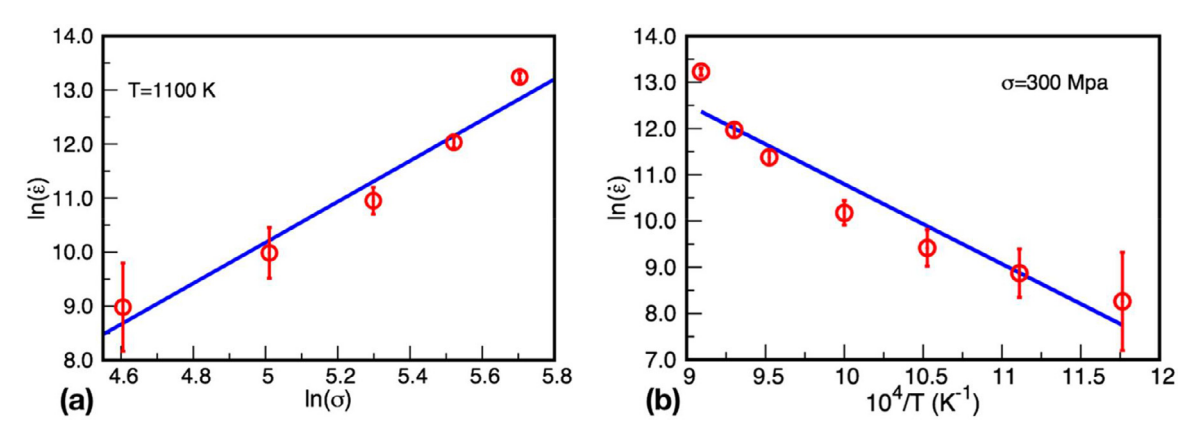


Fig. 8. (a) Log-log plot of steady-state deformation rate versus applied stress at 1100 K used to calculate the stress exponent *n*. (b) Arrhenius plot of steady-state deformation rate under a stress of 300 MPa used to extract the activation energy of the steady-state creep.

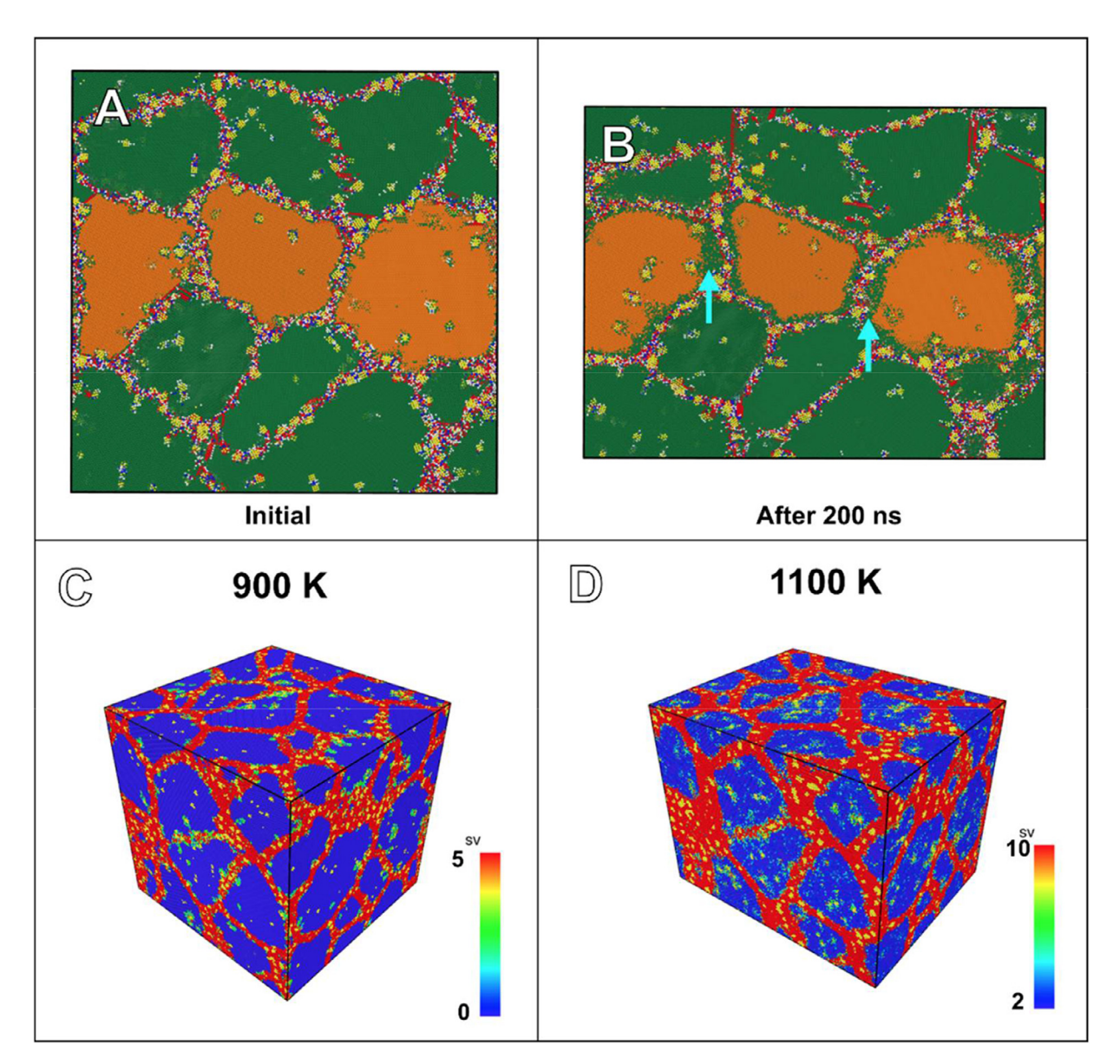
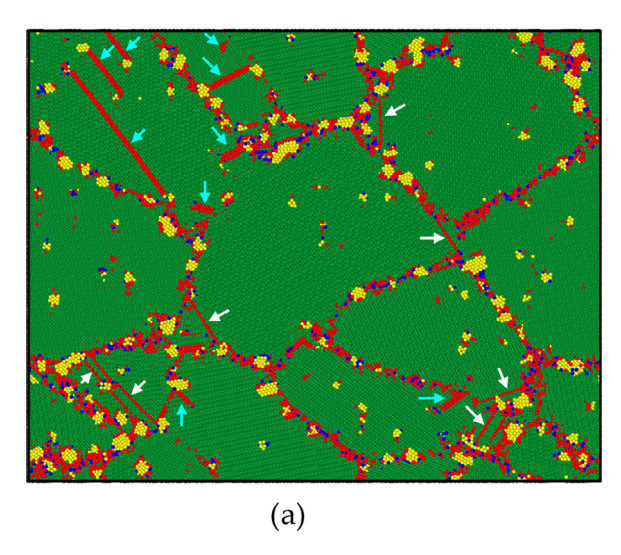


Fig. 9. Two-dimensional slices of three-dimensional atomistic simulations for NC Cu-4at%Ta. (A) before and (B) after tensile creep testing at 1100 K and 300 MPa. The tensile direction is horizontal. The interior atoms of three selected grains are colored in orange. The cyan arrows in (B) indicate the addition of new atomic layers next to the GBs normal to the tensile direction. The slip vector (cv) analysis at (C) 900 K and (D) 1100 K shows that the creep deformation is localized near GBs.



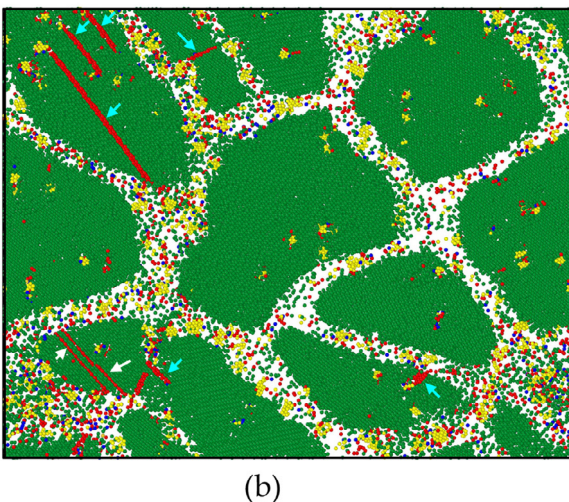


Fig. 10. Demonstration of deformation mechanisms during the simulated tensile creep test at 1100 K under a 300 MPa stress. The tensile axis is horizontal. Both images (a,b) show the same thin slice of the 3D sample after 212 ns of testing. The cyan and white arrows indicate dislocations and twin boundaries, respectively. All atoms were tracked during the test. In (b), the atoms which initially resided in GB regions and later diffused out of the slice were removed from the image. Thus, the white areas along the GBs are caused by extensive GB diffusion. Color coding of the atoms: green – FCC-type atoms, red – HCP-type atoms, blue – BCC-type atoms, yellow – Ta atoms.

sorbed back into neighboring GB regions and did not extend far into the grain interiors. There were very few slip lines passing across the grains at both temperatures, confirming that dislocation slip activity in the grains did not make a significant contribution to the deformation. The most significant slip activity was observed in the vicinity of GBs and triple junctions.

Fig. 10 illustrates the deformation processes in more detail. The images show partial dislocations inside the grains emitted from the GBs. Most of the dislocations are pinned by Ta clusters, which arrested their motion through the grains. Deformation twins are also observed. Fig. 10 additionally illustrated the extensive diffusive transport along the GBs. The impingement of dislocations on Ta clusters inside the grains was observed in the experiments, except this was observed for full dislocations. The absence of full dislocation slip in the simulations could be caused by the smaller grain size and/or shorter observation time. However, both the experiment and the simulations suggest that dislocation activity is not the dominant mechanism of the tensile creep deformation in NC Cu-Ta alloys.

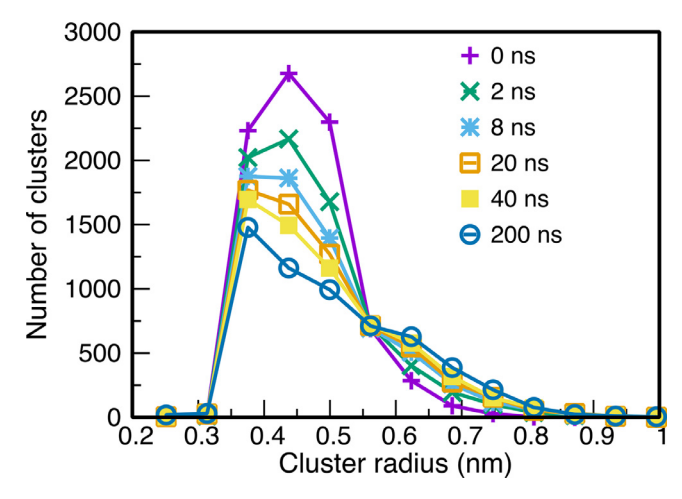


Fig. 11. Size distribution of Ta cluster during creep deformation at $1100~\rm K$ under the stress of $100~\rm MPa$. The key indicates the simulation time.

The Ta cluster size distribution was tracked during the creep process. As one example, Fig. 11 shows the evolution of this distribution during the test at 1100 K under the load of 100 MPa. Similar size distributions were obtained under other testing conditions. The plots show some coarsening of the clusters with time, although their radius remains under 1 nm. Two conclusions follow from these simulations. First, although the size distribution was collected from the entire sample, most of the coarsening is going on among the clusters residing at GBs. This confirms that Ta transport is slow and occurs predominantly along GBs. Second, most of the cluster coarsening happens during the primary creep stage of the deformation, with a much smaller contribution from the steady-state creep. The cluster coarsening is one of the relaxation processes occurring during the primary creep. To support this conclusion, a separate MD simulation was performed at the same temperature and of the same duration. The cluster size evolution was found to closely follow the one observed during the creep test. The final size distribution (after 200 ns, not shown here) is virtually indistinguishable from that shown in Fig. 11.

The experiments have demonstrated the impact of stressrelaxation anneals on the initial strain during the creep tests (Section 3.2 and Fig. 3). To verify this effect and demonstrate its connection with the primary creep, a series of simulations have been conducted that involved interrupted creep tests. The protocol of the tests is presented in Fig. 12(a), showing the individual steps of the simulations labeled by Greek numerals. Step I was a regular 200 ns long tensile creep test starting from an as-prepared sample and deforming it to the onset of steady-state creep. Following the test, the load was removed within 1 ns. The observed 0.5% drop in the strain reflects the fast processes associated with dislocations and some contribution from elasticity. The sample was then reloaded to the initial stress level (300 MPa) and the creep test was continued for another 200 ns (step II). Note that the sample returns to the initial strain and continues to deform in the nearly steady-state regime as if there were no interruptions. This confirms the reversible nature of the processes responsible for the strain drop between the steps I and II. In another simulation (step III), instead of reloading the sample, the stress-free sample was annealed by a 200 ns long MD run. Note that the strain slightly decreased, indicating that thermally activated processes continued to occur to reduce internal stresses. After the stress-free anneal, the sample was subject to another creep test of the usual 200 ns duration and under the same 300 MPa stress (step IV). The creep continued with nearly the same strain rate, but the stain itself was lower than at step II due to the irreversible deformation that oc-

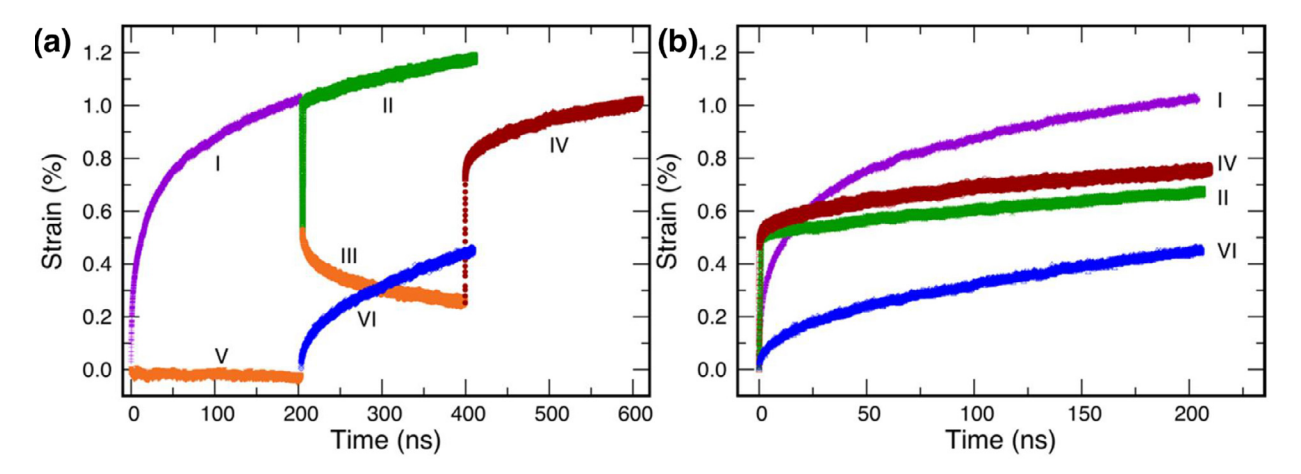


Fig. 12. (a) The protocol of the alternating stress-relaxation tests conducted at 950 K under the stress of 300 MPa. Different steps of the simulation are labeled by Greek numerals as explained in the text. The orange color indicates stress-free simulations. (b) Strain-time curves of the creep simulations shown in (a) are replotted starting from the same initial time. The labeling of the simulation steps and the color coding are the same as in (a).

curred during step III. In yet another simulation, the as-prepared sample was annealed without application of stress (step V), before putting it through a creep test (step VI). This time, the material reached the steady-state regime sooner and with much smaller initial strain. In other words, the primary creep stage was shorter and produced much smaller deformation, because many of the relaxation processes associated with the primary creep have already occurred during the pre-anneal (one of them being the Ta cluster coarsening mentioned above). Fig. 12(b) summarizes the staintime curves during the creep steps I, II, IV and VI plotted relative to the same initial time. The plot clearly demonstrates the effect of anneal-and-reload treatments on the initial creep strain. The simulation results closely correlate with the experimental reloading curves shown in Fig. 3A,C. Although the time scales of the plots are different, the overall behavior seen in the simulations is wellconsistent with the experiment. In particular, it follows from the simulations that anneal at higher temperatures should lead to a decrease in the instantaneous strain, which is confirmed by the experiment (Fig. 3A).

4. Application of the design principle to Ni-Y alloys

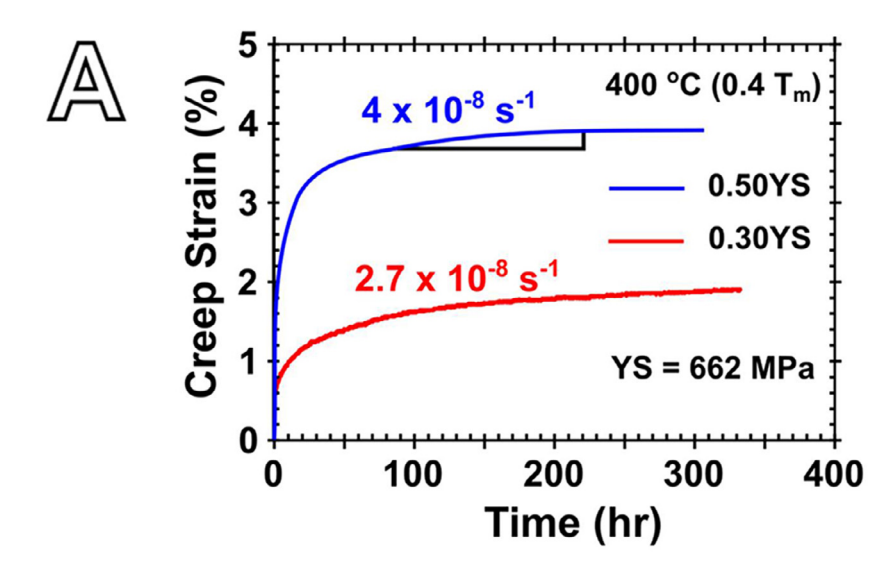
To demonstrate broader applicability of the proposed design principle, a Ni-based alloy containing 5at%Y (referred to as Ni-Y) was developed [38,39]. The Ni-Y alloy has an UFG microstructure with secondary yttrium nitride (YN) inclusions. In addition to the large YN inclusions (~185 nm), small yttrium nano-dispersoids with an average size of approximately 7 nm were observed to be distributed throughout the material and pinning the grain boundaries (see [39]). Because pure NC Ni has a significantly higher yield stress than Cu, it would damage the ECAE processing die. Due to this processing limitation, the temperature at which Ni-Y can be consolidated must be significantly higher, resulting in the UFG (~262 nm grain size) rather than NC microstructure. Previous studies of this alloy have demonstrated that the small yttrium nanodispersoids are responsible for the kinetic pinning of GBs, leading to microstructural stability at relatively high temperatures [38,39]. We have performed a preliminary compression creep characterization of the Ni-Y alloy (compression was used instead of tension due to the sample size limitations discussed earlier [38]). Fig. 13 presents the compression creep response of the Ni-Y alloy at 673 K (0.4 T_m) under the 0.30YS and 0.50YS stresses. Under both levels of applied stress, the steady-state creep rate is on the order of 10^{-8} s⁻¹. This creep rate is much lower than that for pure NC Ni [3] and is comparable to that of Ni-based single crystal superalloys

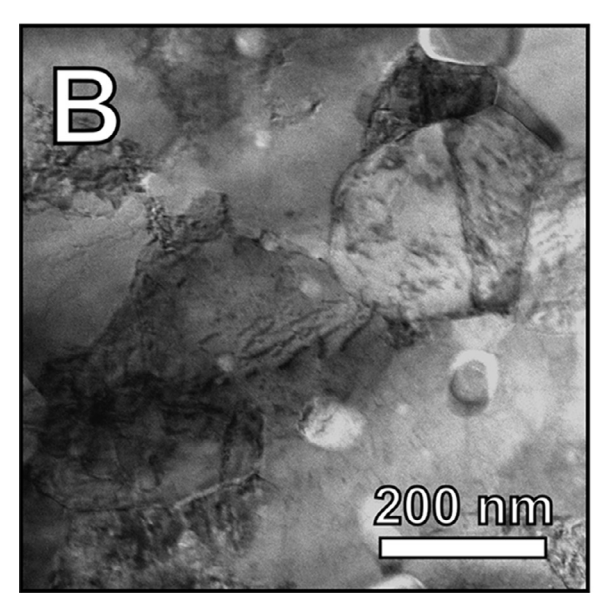
[40]. Post-deformed TEM characterization, Figs. 13 B and C, confirms that there is only a marginal increase in the grain size, with the microstructure still remaining in the UFG regime (see [38] for the initial average grain size). More systematic and detailed studies of this alloy's microstructure and mechanical properties are part of future work. But the results presented here already demonstrate that the approach in which the addition of suitable alloying elements causes the kinetic pinning of GBs is an effective route for stabilizing fine-grained materials and enhancing their structural properties.

5. Discussion

The present study reveals that the Ta nanoclusters play a critical role in explaining the extraordinary resistance of the NC Cu-Ta alloys to tensile creep deformation. It has been found that at temperatures up to 873 K (0.64T_m), most of the usual creep mechanisms are shut down by the Ta nanoclusters through the pinning of GBs and creating obstacles to dislocations inside the grains. Given that lattice diffusion is too slow at these temperatures while the specific GB area is high, this leaves Coble creep [2] the only candidate for the dominant creep mechanism. The Coble creep is controlled by short-circuit diffusion of atoms along the GBs. Although GB diffusion is much faster than lattice diffusion, it is still a thermally activated process that can be slowed down by alloying. Ta is a very slow diffuser both in the lattice and in GBs, which leads to the slow creep deformation rates found in this work. While the experiments do not have the capability to follow the mass transport along the GBs during the creep tests directly, the complementary atomistic simulations provide a direct evidence that the material is dissolved near GBs parallel to the tensile direction, diffuses along the GBs, and gets accreted to GBs oriented perpendicular to the tensile direction. These processes correspond exactly to the Coble creep mechanism.

Dislocation processes also occur during the creep process. Even though they do not directly control the creep rate, they can still contribute to the creep resistance. Dislocation processes are also required as an accommodation mechanism to ensure compatibility of the grain deformations. Evidence has been presented that dislocation motion is slowed down by the Ta clusters. Both the experiments and the simulations have shown that the clusters residing in grain interiors present obstacles to the dislocation glide, see for example the TEM image in Figure S5. These observations are consistent with our previous work [28], where it was also found that at low-to-moderate fractions of T_m, the Ta clusters provide





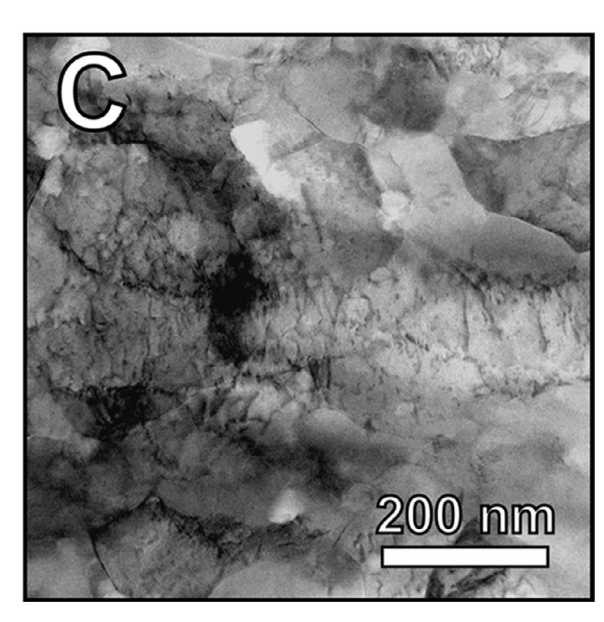


Fig. 13. (A) Compression creep response of the UFG Ni-Y alloy at 673 K (0.39T_m) and 30% (red curve) and 50% (blue curve) of the at-temperature yield stress. (B) and (C) show the post-deformed TEM images of the samples tested under the 0.30YS (B) and 0.50YS (C) loads, respectively.

strong resistance to the dislocation motion. Dislocations stopped by the clusters are unlikely to overcome the obstacles by the climb. The climbing process would require significantly higher homologous temperatures. At temperatures such as 873 K ($0.64T_{\rm m}$), the creep resistance of NC Cu-Ta alloys is primarily caused by the Ta effect on GB mobility and the mass transport along the GBs.

As temperature increases to 973 K $(0.72T_m)$, the misfit strain between the Ta atoms in the clusters and the surrounding Cu matrix decreases (as confirmed by atomistic simulations and the previous experimental study [26]). As a result, at higher temperatures the clusters impose a weaker resistance for the dislocation motion, allowing some of the dislocations to traverse the grains and be annihilated on the opposite side. This opens another creep mechanism that is otherwise blocked at lower temperatures. Dislocations begin to play a more important role in the creep deformation. Nevertheless, the steady-state creep rate still remains unusually low and is comparable to that observed in Ni-based superalloys (see Fig. 3A).

In this work, the atomistic simulations were integrated with the experiment as a complementary tool. Both the experimental and simulation approaches have their limitations. For example, the simulated grain size is much smaller than the experimental. The MD creep testing time is much shorter, and the creep rate is much higher than in the experiment. These differences with the experimental conditions are caused by the limited size and time scales currently accessible by MD simulations. On the other hand, simulations provide full access to all atomic-level processes, such as GB sliding, atomic transport along GBs, and the detailed time evolution of the Ta nanoclusters during the creep tests. This information provides significant insights into the creep mechanisms on the microscopic level. The ability to track atomic fluxes enabled us to provide direct evidence of grain elongation by GB diffusion, intercluster diffusion of Ta atoms along the GBs, as well as GB sliding and the restrain of dislocation motion by the intra-granular clusters. These insights have a local character and are not expected to depend sensitively on the grain size as long as the latter is on the 10-100 nm length scale.

To put this work in a broader perspective, there are several approaches to stabilizing nanostructures by preventing or at least reducing the grain growth. The best known of them are the thermodynamic mechanism and the kinetic mechanism. Stabilization by the thermodynamic mechanism is achieved through a reduction of

the GB free energy γ by solute segregation [41–47]. Smaller values of γ reduce the capillary force which drives the grain growth, preserving the nano-scale grains up to higher temperatures. In fact, it has been suggested that one can produce a thermodynamically stable NC material by reaching a minimum of the total free energy [42,43,46,48-53]. The kinetic stabilization is achieved by reducing the GB mobility. One way to reach this goal is to introduce solutes that strongly segregate to GBs and reduce their mobility by the solute drag effect [54-57]. Another, and more effective approach, is to alloy the material with immiscible elements that precipitate in the form of stable nanophases or nanoclusters. These small precipitates pin the GBs in place by the Zener pinning mechanism [57-63]. As was demonstrated in the previous work [63,64], the extraordinary structural stability of the Cu-Ta alloys is caused by the Zener pinning mechanism, with the Ta nanoclusters playing the role of the pinning centers.

Alloying has traditionally been used as an effective means to improve the properties of high-temperature, high-strength of structural materials. For example, the creep resistance of Ni-based superalloys can be improved by alloying with slow-diffusing elements such as Re and W [65,66]. However, this strategy is fundamentally different from the one pursued in this work. The mentioned elements reduce the diffusion rate in the crystalline lattice [67,68]. They primarily affect the creep process via the dislocation glide, dislocation climb, and possibly other process controlled by lattice diffusion. This is in contrast to the present design principle, where the goal is to stabilize a nano-scale microstructure by pinning the GBs and reducing the rate of GB diffusion.

Overall, the present work demonstrates a pathway toward the development of stronger NC materials exhibiting a spectrum of highly improved properties such as high strength, ductility and creep resistance, with an eye towards high-temperature applications such as turbines. The proposed approach is not exclusive to the Cu-Ta system. It can be extended to other materials systems by introducing nanoclusters/nanophases that can kinetically stabilize the microstructure and preserve the mechanical strength up to high temperatures.

6. Conclusions

In summary, the results demonstrate that stabilizing fine grain sizes by nanoclusters can lead to exceptional mechanical properties that deviate from the traditional deformation mechanisms. As an example, the NC Cu-3Ta alloy tested under tensile creep conditions up to the temperature of 873 K (0.64T_m) displays a highly unusual behavior, including the absence of any appreciable steadystate creep deformation normally observed in almost all materials. The Ta nanoclusters distributed throughout the microstructure are extremely effective in stabilizing the microstructure and inhibiting the dislocation-based creep mechanisms. The general conclusion of this work is that the alloying of pure NC metals with immiscible solutes that precipitate in the form of nanoclusters is an extremely effective way of achieving microstructural stability and drastically improved mechanical properties. It is expected that this work will promote research efforts focused on the design of high-performance bulk NC materials suitable for high-temperature structural applications.

Declaration of Competing Interest

The authors declare no competing financial interests.

Acknowledgement

This work was supported by Army Research Laboratory award number W911NF-15-2-0038 and the National Science Foundation

award numbers 1663287 and 1810431. R. K. K and Y. M. were supported by the U.S. Army Research Office under contract number W911NF-15-1-007.

Data and materials availability: The data that support the findings are available from the corresponding authors upon request.

Supplementary materials

Supplementary material associated with this article can be found, in the online version, at doi:10.1016/j.actamat.2020.08.020.

References

- [1] M.F. Ashby, A first report on deformation-mechanism maps, Acta Metall. 20 (1972) 887–897, doi:10.1016/0001-6160(72)90082-X.
- [2] R. Coble, A model for boundary diffusion controlled creep in polycrystalline materials, J. Appl. Phys. 34 (1963) 1679–1682.
- [3] F.A. Mohamed, Y. Li, Creep and superplasticity in nanocrystalline materials: current understanding and future prospects, Mater. Sci. Eng. A 298 (2001) 1– 15, doi:10.1016/S0928-4931(00)00190-9.
- [4] A.H. Chokshi, Unusual stress and grain size dependence for creep in nanocrystalline materials, Scr. Mater. 61 (2009) 96–99, doi:10.1016/j.scriptamat.2009.03.
- [5] N. Yagi, A. Rikukawa, H. Mizubayashi, H. Tanimoto, Experimental tests of the elementary mechanism responsible for creep deformation in nanocrystalline gold, Phys. Rev. B. 74 (2006) 144105.
- [6] K.A. Darling, M. Rajagopalan, M. Komarasamy, M.A. Bhatia, B.C. Hornbuckle, R.S. Mishra, K.N. Solanki, Extreme creep resistance in a microstructurally stable nanocrystalline alloy, Nature 537 (2016) nature 19313, doi:10.1038/nature19313.
- [7] J. Cormier, Not so creepy under stress, Nature 537 (2016) 315–316, doi:10.1038/ 537315a
- [8] B.C. Hornbuckle, T. Rojhirunsakool, M. Rajagopalan, T. Alam, G.P.P. Pun, R. Banerjee, K.N. Solanki, Y. Mishin, L.J. Kecskes, K.A. Darling, Effect of Ta solute concentration on the microstructural evolution in immiscible Cu-Ta alloys, JOM 67 (2015) 2802–2809, doi:10.1007/s11837-015-1643-x.
- [9] V.H. Hammond, T.L. Luckenbaugh, M. Aniska, D.M. Gray, J.A. Smeltzer, B.C. Hornbuckle, C.J. Marvel, K.N. Solanki, T. Schmitz, K.A. Darling, An insight into machining of thermally stable bulk nanocrystalline metals, Adv. Eng. Mater. 20 (2018) 1800405, doi:10.1002/adem.201800405.
- [10] M. Rajagopalan, K. Darling, C. Kale, S. Turnage, R. Koju, B. Hornbuckle, Y. Mishin, K. Solanki, Nanotechnology enabled design of a structural material with extreme strength as well as thermal and electrical properties, Mater. Today 31 (2019) 10–20.
- [11] B.C. Hornbuckle, C. Kale, S. Srinivasan, T.L. Luckenbaugh, K.N. Solanki, K.A. Darling, Revealing cryogenic mechanical behavior and mechanisms in a microstructurally-stable, immiscible nanocrystalline alloy, Scr. Mater. 160 (2019) 33–38, doi:10.1016/j.scriptamat.2018.09.035.
- [12] B.C. Hornbuckle, C.L. Williams, S.W. Dean, X. Zhou, C. Kale, S.A. Turnage, J.D. Clayton, G.B. Thompson, A.K. Giri, K.N. Solanki, K.A. Darling, Stable microstructure in a nanocrystalline copper-tantalum alloy during shock loading, Commun. Mater. 1 (2020) 1–6, doi:10.1038/s43246-020-0024-3.
- [13] S. Srinivasan, C. Kale, B.C. Hornbuckle, K.A. Darling, M.R. Chancey, E. Hernández-Rivera, Y. Chen, T.R. Koenig, Y.Q. Wang, G.B. Thompson, K.N. Solanki, Radiation tolerance and microstructural changes of nanocrystalline Cu-Ta alloy to high dose self-ion irradiation, Acta Mater. 195 (2020) 621–630, doi:10.1016/j.actamat.2020.05.061.
- [14] G.P. Pun, K. Darling, L. Kecskes, Y. Mishin, Angular-dependent interatomic potential for the Cu-Ta system and its application to structural stability of nano-crystalline alloys, Acta Mater. 100 (2015) 377-391.
- [15] S. Plimpton, Fast parallel algorithms for short-range molecular dynamics, J. Comput. Phys. 117 (1995) 1–19, doi:10.1006/jcph.1995.1039.
- [16] V.I. Yamakov, Parallel Grand Canonical Monte Carlo (ParaGrandMC) Simulation Code, 2016 https://software.nasa.gov/software/LAR-18773-1.
- [17] Y. Mishin, Calculation of the γ/γ' interface free energy in the Ni–Al system by the capillary fluctuation method, Model. Simul. Mater. Sci. Eng. 22 (2014) 045001.
- [18] A.G. Frøseth, H. Van Swygenhoven, P.M. Derlet, Developing realistic grain boundary networks for use in molecular dynamics simulations, Acta Mater. 53 (2005) 4847–4856, doi:10.1016/j.actamat.2005.06.032.
- [19] A. Leonardi, M. Leoni, P. Scardi, Atomistic modelling of polycrystalline microstructures: An evolutional approach to overcome topological restrictions, Comput. Mater. Sci. 67 (2013) 238–242, doi:10.1016/j.commatsci.2012.09.013.
- [20] T. Xu, S. Sarkar, M. Li, Y. Wang, Quantifying microstructures in isotropic grain growth from phase field modeling: Topological properties, Acta Mater 61 (2013) 2450–2459. doi:10.1016/j.actamat.2013.01.017.
- [21] A. Prakash, M. Hummel, S. Schmauder, E. Bitzek, Nanosculpt: A methodology for generating complex realistic configurations for atomistic simulations, MethodsX 3 (2016) 219–230, doi:10.1016/j.mex.2016.03.002.
- [22] Z. Trautt, A. Adland, A. Karma, Y. Mishin, Coupled motion of asymmetrical tilt grain boundaries: Molecular dynamics and phase field crystal simulations, Acta Mater. 60 (2012) 6528–6546.

- [23] A. Stukowski, Visualization and analysis of atomistic simulation data with OVITO-the Open Visualization Tool, Model. Simul. Mater. Sci. Eng. 18 (2009) 015012
- [24] J.F. Panzarino, T.J. Rupert, Tracking microstructure of crystalline materials: a post-processing algorithm for atomistic simulations, Jom 66 (2014) 417–428.
- [25] M. Bhatia, M. Rajagopalan, K. Darling, M. Tschopp, K. Solanki, The role of Ta on twinnability in nanocrystalline Cu-Ta alloys. Mater. Res. Lett. 5 (2017) 48-54.
- [26] M. Rajagopalan, K. Darling, S. Turnage, R.K. Koju, B. Hornbuckle, Y. Mishin, K.N. Solanki, Microstructural evolution in a nanocrystalline Cu-Ta alloy: a combined in-situ TEM and atomistic study, Mater. Des. 113 (2017) 178–185, doi:10.1016/j.matdes.2016.10.020.
- [27] S.A. Turnage, M. Rajagopalan, K.A. Darling, P. Garg, C. Kale, B.G. Bazehhour, I. Adlakha, B.C. Hornbuckle, C.L. Williams, P. Peralta, K.N. Solanki, Anomalous mechanical behavior of nanocrystalline binary alloys under extreme conditions. Nat. Commun. 9 (2018) 2699. doi:10.1038/s41467-018-05027-5.
- [28] C. Kale, S. Turnage, P. Garg, I. Adlakha, S. Srinivasan, B.C. Hornbuckle, K. Darling, K.N. Solanki, Thermo-mechanical strengthening mechanisms in a stable nanocrystalline binary alloy a combined experimental and modeling study, Mater. Des. 163 (2019) 107551, doi:10.1016/j.matdes.2018.107551.
- [29] P.G. Sanders, J. Eastman, J. Weertman, Elastic and tensile behavior of nanocrystalline copper and palladium, Acta Mater. 45 (1997) 4019–4025.
- [30] P. Caron, T. Khan, Improvement of creep strength in a nickel-base single-crystal superalloy by heat treatment, Mater. Sci. Eng. 61 (1983) 173–184.
- [31] R. Reed, D. Cox, C. Rae, Damage accumulation during creep deformation of a single crystal superalloy at 1150 C, Mater. Sci. Eng. A. 448 (2007) 88–96.
- [32] S. Tian, X. Zhu, J. Wu, H. Yu, D. Shu, B. Qian, Influence of temperature on stacking fault energy and creep mechanism of a single crystal nickel-based super-
- alloy, J. Mater. Sci. Technol. 32 (2016) 790–798, doi:10.1016/j.jmst.2016.01.020. [33] A.H. Cottrell, V. Aytekin, Andrade's creep law and the flow of zinc crystals, Nature 160 (1947) 328–329, doi:10.1038/160328a0.
- [34] C. Smith, A theory of transient creep in metals, Proc. Phys. Soc. 61 (1948) 201.
- [35] A.K. Mukherjee, An examination of the constitutive equation for elevated temperature plasticity, Mater. Sci. Eng. A. 322 (2002) 1–22.
- [36] T. Surholt, C. Herzig, Grain boundary self-diffusion in Cu polycrystals of different purity, Acta Mater. 45 (1997) 3817–3823, doi:10.1016/S1359-6454(97) 00037-2.
- [37] I. Kaur, Y. Mishin, W. Gust, Fundamentals of Grain and Interphase Boundary Diffusion, 3rd ed., Wiley, 1995 https://www.wiley.com/en-us/ Fundamentals+of+Grain+and+Interphase+Boundary+Diffusion%2C+3ed+ Revised+and+Enlarged+Edition-p-9780471938194.
- [38] K.A. Darling, L.J. Kecskes, M. Atwater, J. Semones, R.O. Scattergood, C.C. Koch, Thermal stability of nanocrystalline nickel with yttrium additions, J. Mater. Res. 28 (2013) 1813–1819, doi:10.1557/jmr.2013.9.
- [39] S. Srinivasan, C. Kale, B.C. Hornbuckle, K.A. Darling, P. Peralta, K.N. Solanki, Thermomechanical response of an ultrafine-grained nickel-yttrium alloy, Scr. Mater. 187 (2020) 434–438, doi:10.1016/j.scriptamat.2020.06.068.
- [40] T.M. Pollock, S. Tin, Nickel-based superalloys for advanced turbine engines: chemistry, microstructure, and properties, J. Propuls. Power. 22 (2006) 361–374.
- [41] C.C. Koch, R.O. Scattergood, K.A. Darling, J.E. Semones, Stabilization of nanocrystalline grain sizes by solute additions, J. Mater. Sci. 43 (2008) 7264– 7272, doi:10.1007/s10853-008-2870-0.
- [42] T. Chookajorn, H.A. Murdoch, C.A. Schuh, Design of stable nanocrystalline alloys, Science 337 (2012) 951–954, doi:10.1126/science.1224737.
- [43] H.A. Murdoch, C.A. Schuh, Stability of binary nanocrystalline alloys against grain growth and phase separation, Acta Mater. 61 (2013) 2121–2132, doi:10. 1016/j.actamat.2012.12.033.
- [44] M. Saber, H. Kotan, C.C. Koch, R.O. Scattergood, A predictive model for thermodynamic stability of grain size in nanocrystalline ternary alloys, J. Appl. Phys. 114 (2013) 103510, doi:10.1063/1.4821040.
- [45] M. Rajagopalan, M.A. Tschopp, K.N. Solanki, Grain boundary segregation of interstitial and substitutional impurity atoms in alpha-iron, JOM 66 (2014) 129–138, doi:10.1007/s11837-013-0807-9.

- [46] A.R. Kalidindi, C.A. Schuh, Stability criteria for nanocrystalline alloys, Acta Mater. 132 (2017) 128–137. doi:10.1016/j.actamat.2017.03.029.
- [47] K.A. Darling, M.A. Tschopp, B.K. VanLeeuwen, M.A. Atwater, Z.K. Liu, Mitigating grain growth in binary nanocrystalline alloys through solute selection based on thermodynamic stability maps, Comput. Mater. Sci. 84 (2014) 255–266, doi:10. 1016/j.commatsci.2013.10.018.
- [48] J.R. Trelewicz, C.A. Schuh, Grain boundary segregation and thermodynamically stable binary nanocrystalline alloys, Phys. Rev. B. 79 (2009) 094112, doi:10.1103/PhysRevB.79.094112.
- [49] T. Chookajorn, C.A. Schuh, Thermodynamics of stable nanocrystalline alloys: A Monte Carlo analysis, Phys. Rev. B. 89 (2014) 064102, doi:10.1103/PhysRevB.89. 064102.
- [50] A.R. Kalidindi, T. Chookajorn, C.A. Schuh, Nanocrystalline materials at equilibrium: a thermodynamic review, JOM 67 (2015) 2834–2843, doi:10.1007/ s11837-015-1636-9
- [51] J. Weissmüller, Alloy thermodynamics in nanostructures, J. Mater. Res. 9 (1994)4–7. doi:10.1557/IMR.1994.0004.
- [52] R. Kirchheim, Reducing grain boundary, dislocation line and vacancy formation energies by solute segregation: II. Experimental evidence and consequences, Acta Mater. 55 (2007) 5139–5148, doi:10.1016/j.actamat.2007.05.033.
- [53] R. Kirchheim, Reducing grain boundary, dislocation line and vacancy formation energies by solute segregation. I. Theoretical background, Acta Mater. 55 (2007) 5129–5138, doi:10.1016/j.actamat.2007.05.047.
- [54] J.W. Cahn, The impurity-drag effect in grain boundary motion, Acta Metall. 10 (1962) 789–798, doi:10.1016/0001-6160(62)90092-5.
- [55] N. Ma, S.A. Dregia, Y. Wang, Solute segregation transition and drag force on grain boundaries, Acta Mater. 51 (2003) 3687–3700, doi:10.1016/ S1359-6454(03)00184-8.
- [56] I. Toda-Caraballo, C. Capdevila, G. Pimentel, C.G. De Andrés, Drag effects on grain growth dynamics, Comput. Mater. Sci. 68 (2013) 95–106, doi:10.1016/j. commatsci.2012.10.012.
- [57] F. Abdeljawad, P. Lu, N. Argibay, B.G. Clark, B.L. Boyce, S.M. Foiles, Grain boundary segregation in immiscible nanocrystalline alloys, Acta Mater. 126 (2017) 528–539, doi:10.1016/j.actamat.2016.12.036.
- [58] E. Nes, N. Ryum, O. Hunderi, On the Zener drag, Acta Metall. 33 (1985) 11–22, doi:10.1016/0001-6160(85)90214-7.
- [59] W.-B. Li, K.E. Easterling, The influence of particle shape on Zener drag, Acta Metall. Mater. 38 (1990) 1045–1052, doi:10.1016/0956-7151(90)90177-1.
- [60] P.A. Manohar, M. Ferry, T. Chandra, Five decades of the zener equation, ISIJ Int. 38 (1998) 913–924, doi:10.2355/isijinternational.38.913.
- [61] M. Miodownik, E.A. Holm, G.N. Hassold, Highly parallel computer simulations of particle pinning: Zener vindicated, Scr. Mater. 42 (2000) 1173–1177, doi:10. 1016/S1359-6462(00)00354-7.
- [62] C.L.D. Prinzio, E. Druetta, O.B. Nasello, More about Zener drag studies with Monte Carlo simulations, Model. Simul. Mater. Sci. Eng. 21 (2013) 025007, doi:10.1088/0965-0393/21/2/025007.
- [63] R.K. Koju, K.A. Darling, L.J. Kecskes, Y. Mishin, Zener pinning of grain boundaries and structural stability of immiscible alloys, JOM (2016) 1–9, doi:10.1007/ s11837-016-1899-9.
- [64] R.K. Koju, K.A. Darling, K.N. Solanki, Y. Mishin, Atomistic modeling of capillary-driven grain boundary motion in Cu-Ta alloys, Acta Mater. 148 (2018) 311–319, doi:10.1016/j.actamat.2018.01.027.
- [65] R.C. Reed, The Superalloys: Fundamentals and Applications, Cambridge University Press, 2008.
- [66] M. Huang, J. Zhu, An overview of rhenium effect in single-crystal superalloys, Rare Met. 35 (2016) 127–139.
- [67] M. Grabowski, J. Rogal, R. Drautz, Kinetic Monte Carlo simulations of vacancy diffusion in nondilute Ni-X (X = Re, W, Ta) alloys, Phys. Rev. Mater. 2 (2018) 123403, doi:10.1103/PhysRevMaterials.2.123403.
- [68] S. Gao, Z. Yang, M. Grabowski, J. Rogal, R. Drautz, A. Hartmaier, Influence of excess volumes induced by re and w on dislocation motion and creep in ni-base single crystal superalloys: a 3D discrete dislocation dynamics study, Metals 9 (2019) 637, doi:10.3390/met9060637.